Supplementary materials: Optical valley Hall effect for highly valley-coherent exciton-polaritons in an atomically thin semiconductor

Nils Lundt, Łukasz Dusanowski, Evgeny Sedov, Petr Stepanov, Mikhail M. Glazov, Sebastian Klembt, Martin Klaas, Johannes Beierlein, Ying Qin, Sefaattin Tongay, Maxime Richard, Alexey V. Kavokin, Sven Höfling and Christian Schneider

S1: Characteristics of mechanically assembled DBR-DBR micro-cavities

Here, we present the characteristics of a separate mechanically assembled DBR-DBR micro-cavity without $MoSe_2$ monolayer. Figure S1a shows the dispersion relation of such a cavity measured in reflectivity. We extract an effective cavity mass of $1.23 \cdot 10^{-5}\, m_e$, where m_e is the free electron mass. Figure S1b presents the resonance feature of the spectrum taken with a high-resolution optical grating (1200l/mm) at $k_{||} = 0\ \mu m^{-1}$. From this we extract a line width of 0.163 nm, which is equivalent to a Q-factor of 4600. The effective cavity length is estimated to be on the order of 400 nm based on transfer matrix calculations.

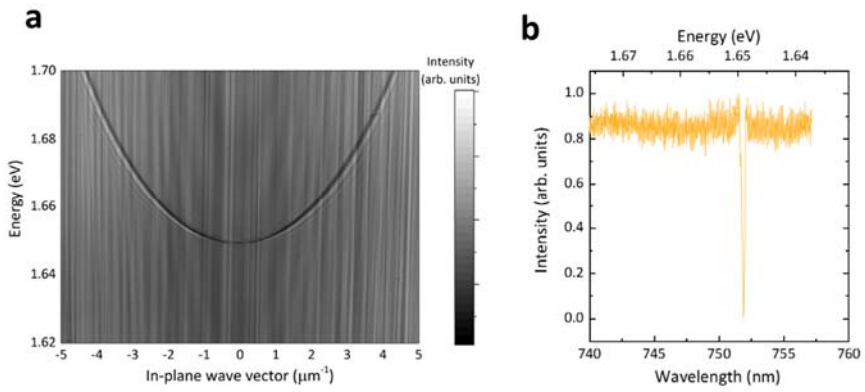

Figure S1: a) Dispersion relation of a mechanically assembled, empty cavity, measured in reflectivity. b) Reflectivity line spectrum at zero in-plane momentum.

S2: Evidence for the strong coupling regime in our microcavity: Part I

In Fig. 1d of the main text, we plot the dispersion relation of the lower polariton branch, acquired under non-resonant pumping, together with the coupled oscillator fit to the data. We will now provide evidence, that the luminescence occurs in the strong coupling regime. In Fig. S2a we reproduce the spectrum plotted in Fig. 1d in the main text. In order to fit the observed lower polariton branch, we applied the conventional two-coupled oscillator model. The cavity energy for this model was taken from the anti-crossing experiment presented in the supplementary section S4 (1.642 eV), hence it is not a free fitting parameter. For the best fitting result, the exciton energy, which entered the model, was assumed to be 5 meV above the value measured in Figure 1c in the main text. The slight difference can be explained by an uneven influence of the PMMA layer and/or slight strain conditions. Still, it is within the inhomogeneous broadening. The calculated dispersion relation for the lower branch, shown

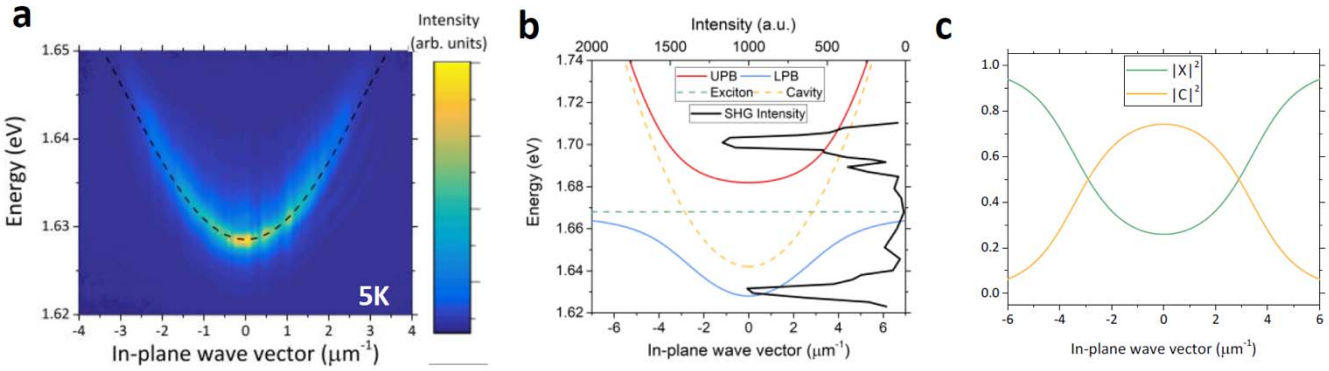

Figure S2: a) Photoluminescence from the lower polariton state (non-resonant pumping). The black, dashed line is the result of the coupled oscillator fit. b) Plot of the full two-coupled-oscillator model for the measured polariton: dispersion relation for upper and lower polariton modes are shown in solid blue and red lines. The uncoupled exciton (red, dashed line) and cavity (black, dashed line) are also indicated here. Along with the coupled oscillator fit, we depict the result of a scanning second harmonic generation experiment. We find, that the SHG signal corresponds with the predicted polariton states of the coupled harmonic oscillator mode, and furthermore, the SHG intensity scales with the photonic Hopfield coefficient of the LPB and UPB states b) Absolute values squared of exciton- and photon Hopfield coefficients for the lower polariton branch.

in Fig. S2a and Fig. 1d (main text) yields the best match to the experimental data for a normal mode splitting of 46 meV. The Hopfield coefficients of the LPB are plotted in Fig. S2c as a function of the in-plane wave vector, showing that the lower polariton is predominantly photonic with a cavity fraction of 74 %.

In Fig. S2b we plot the complete coupled oscillator dispersion relation (corresponding with the fitting result shown in Fig. S2a). Along with the modelled dispersion relation, we plot the result of a scanning second harmonic generation (SHG) experiment. Here, we tuned our linearly polarized near infrared laser (2 ps, 76 MHz) between 1450 and 1528 nm, and recorded the second harmonic signal generated from the polariton resonances. The SHG intensity generated from the sample is plotted alongside with the calculated dispersion relation in Fig S2b as a function of twice the pump energy. First, we would like to state, while the broken inversion symmetry of the TMDC crystal enforces SHG, similar effects have previously been observed in GaAs microcavities in the strong coupling regime (ref. 40, main text).

In our experiment, we find a strong enhancement of the SHG signal when the laser is scanned over the lower polariton branch. In particular, the SHG signal acquires a significant intensity for polariton states with high photonic Hopfield coefficients, near the ground state. This correlation of SHG and the photonic Hopfield coefficient has been observed in previous studies (see Ref 1), where the SHG intensity was found to be most intense for polaritonic resonances with photonic fractions > 50 %. For frequencies around the anti-crossing region, the SHG signal is not observable in our experiment, but importantly, we observe a second peak in the SHG signal where our coupled oscillator model predicts the upper polariton branch. While weak SHG signals indeed can be observed starting from the lowest energy states of the UPB (with a large excitonic fraction), again, the SHG intensity increases for higher energy states in the UPB with a larger photonic fraction. This, correspondingly, reflects the direct correlation of SHG intensity and the photon Hopfield coefficient previously found in GaAs microcavities in the strong coupling regime.

To summarize, our measured dispersion relation of the lower polariton branch can be quantitatively reproduced by a coupled oscillator dispersion, and at the same time, we observe significant SHG intensity when we scan our infrared laser through the resonances of the LPB as well as the predicted UPB, showing the expected dependency on the photonic Hopfield coefficient. Thus, we believe that our data provide direct evidence for the strong coupling regime in our device.

S3: Evidence for the Strong coupling regime in our microcavity: Part II

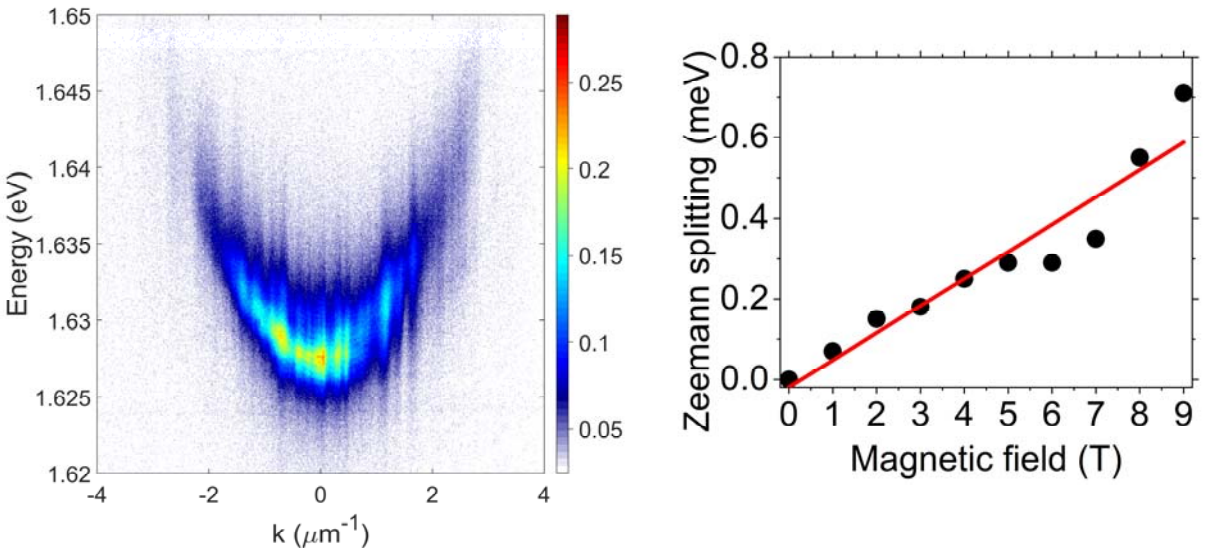

Figure S3: a) Photoluminescence from the lower polariton state (non-resonant pumping) in the magnetic cryostat. b) Extracted energy splitting of the polariton ground state as a function of applied magnetic field. The extracted Zeeman-Splitting evidences the matter-contribution to our quasi-particles, and thus proves strong coupling conditions in our device.

Further evidence for the presence of strong coupling conditions in our microcavity is reflected by its response to an external magnetic field. As a result of coherent light-matter coupling, exciton-polaritons react to magnetic fields applied in the Faraday geometry, and exhibit a characteristic Zeeman-splitting. For exciton-polaritons emerging from TMDC crystals, the diamagnetic contribution can usually be safely neglected for magnetic fields < 30 T [2]. Indeed, the Zeeman-splitting for TMDC-based exciton polaritons has been recently observed[3], in closest analogy to experiments conducted on III-V based microcavities[4]. Thus, we have studied our microcavity in the presence of an external magnetic field up to 9T, and extracted the circular polarization splitting of the polariton ground state (Fig. S3a) as a function of the magnetic field strength. We observe a clear emergence of the polaritonic Zeeman-effect (Fig. S3b), which can only be explained by the presence of strong coupling conditions in our device. Indeed, in the absence of excitonic fraction in the observed mode, no Zeeman effect occurs. We note, that a full quantitative treatment of the effect is given in Ref. 3. Here, we can extract a polaritonic g-factor of 1.16, which transposes into an excitonic g-factor of 4.48 by applying the linear fitting procedure to our data. Here, $\Delta E_R = |X|^2\, g\ \mu_B\, B$. Here, $|X|^2$ denotes the excitonic Hopfield coefficient (0.26). We would like to note, that a g-factor of 4.48 for the valley-exciton is in excellent agreement with the literature (see Refs 2 and 3, as well as references therein).

S4: Evidence for the Strong coupling regime in our microcavity: Part III

Since the upper polariton branch is not well-observable under non-resonant optical excitation (photoluminescence), in addition to the SHG experiment in S2 section, a white light reflectivity measurement was carried out, which should reveal the upper polariton branch as its absorption does not require the population of the UPB. Figure S4a shows reflectivity spectra recorded at various temperatures from 10 K to 170 K. The observed resonances show a distinct anti-crossing behavior for a crossing point at about 125 K. The observed normal mode splitting is 30 (±2) meV at this temperature.

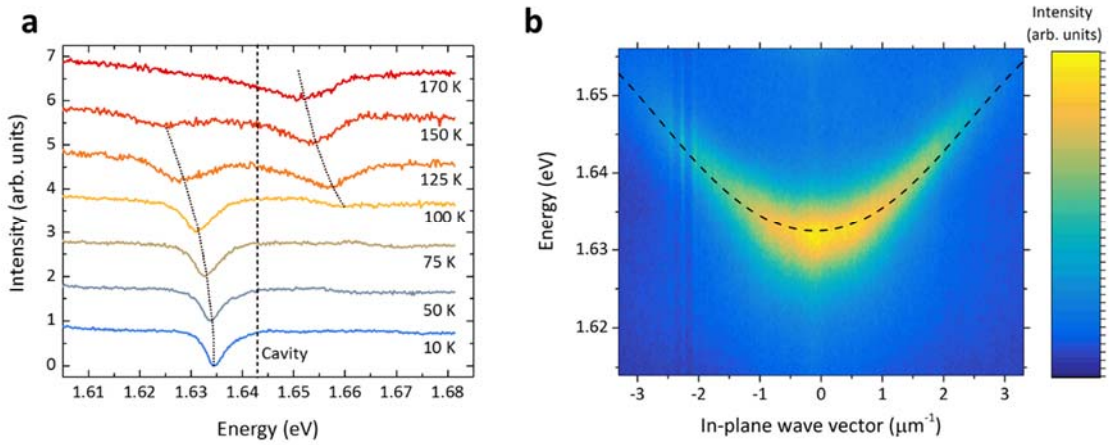

Figure S4: a) Reflectivity spectra of the full system at various temperatures. The exciton tuned in the temperature series, revealing a distinct anti-crossing behavior. Upper and lower polariton branch as well as the cavity are indicated as guide to the eye. b) Lower polariton dispersion relation measured at 5 K the in photoluminescence. The corresponding two-coupled-oscillator model is indicated by the black-dashed line.

The extracted cavity resonance is 17 meV below the measured empty cavity, presented in Figure 1c in the main text. It should be noted that the latter measurement was taken 20 – 30 µm away from the monolayer position. Thus, slight fluctuations of the PMMA thickness and also the real part of the monolayer refractive index explain the shifted cavity resonance. Figure S4b shows the dispersion of the lower polariton branch measured at 5 K in photoluminescence, and the according coupled oscillator fit (using the same parameters as extracted in Fig. S2a). The best agreement between theory and experiment is achieved for a normal mode splitting of 34 meV. This is explained with an increasing exciton oscillator strength towards lower temperature, which in turn increases the normal mode splitting. This observation is in quantitative agreement with the temperature dependent normal mode splitting simulated in reference[5]. It should be noted that the measurements presented in Fig. S4a and Fig S4b were acquired several months after the PL dispersions presented in Figure 1 in the main text and the study in Fig S2. Here, we have extracted a slightly reduced normal mode splitting (34 meV), as compared to the data analysis corresponding to Fig. 1 (46 meV, see also suppl. S2). We attribute this difference to a slight modification of the charging state in the monolayer, which has been recently shown to directly influence the coupling strength on such a quantitative level [6,7].

To summarize, we could fully map out the full anticrossing curve of the two polariton branches in white-light reflection measurements on our device, adding further direct evidence for the presence of strong coupling conditions in our sample.

S5: Quantization of perpendicular modes

The quantization of perpendicular modes of an elongated cavity wire can be calculated according to [8]:

$$E_m(k_x) = \sqrt{E_C^2 + \frac{h^2 c^2}{4\,\pi^2 \varepsilon_{eff}}\left[k_x^2 + \frac{(m+1)^2\,\pi^2}{L_y^2}\right]},$$

where $E_m(k_x)$ is the energy dispersion of the mode with the quantization index m (m = 0,1,2,…) along the X direction (that corresponds to the elongated monolayer axis), ε_{eff} is the effective dielectric constant and L_y is the confinement length along the Y-axis (perpendicular to the long axis X). Using the monolayer width (8 µm) as an input, the measured ground mode energy, the difference between $E_1(k_x)$ and $E_0(k_x)$ is calculated to be 3.0 meV, which is in excellent agreement with the measured quantization energy of 2.7 meV extracted from the data set shown in Fig. 1e in the main text.

S6: SHG on $MoSe_2$ cavity polaritons

In order to study the two photon absorption process in our system in more detail, we excited the structure slightly above the ground state with a laser wavelength of 1514 nm, yielding a SHG signal at 757 nm with a linewidth of 1.5 nm/3.3 meV (see supplementary S7). Figure S5a shows the resulting emission spectrum acquired under such excitation. Besides the SHG emission peak at 757 nm, the spectrum is dominated by the emission from quantized polaritonic resonances that have lower

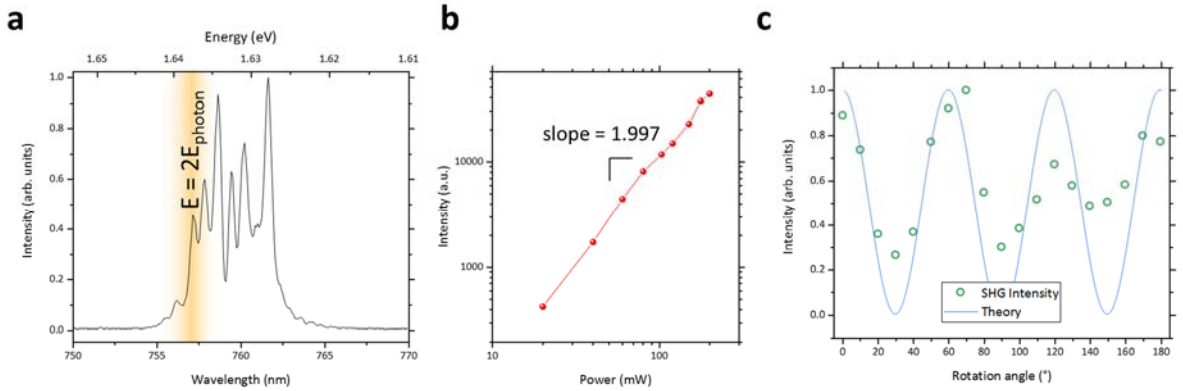

Figure S5: Two-photon excitation: (a) Emission spectrum under slightly off-resonant excitation at 1514 nm, showing emission features at the SHG energy (marked in orange), but also at lower energies. (b) Double-logarithmic plot of the SHG intensity (intensity from the SHG energy feature only) versus excitation power. (c) Dependence of the SHG intensity on the orientation of the exciting lights linear polarization. (b and c) error bars correspond to symbol size.

energies than the SHG signal. In fact, the lowest lying resonance coincides with the ground state of the lower polariton branch. This indicates that exciton-polaritons, which are resonantly excited via two-photon absorption, relax in our system towards their ground-state quite efficiently. We believe that luminescence from these states is a result of a two-photon absorption interband transition since SHG should only be observable at double the excitation energy. In principle, such a transition is spin-forbidden for a 1s exciton (and the corresponding exciton-polariton); however, the intermixing with 2p states allows a two-photon interband transition into this state[9,10]. Following reference[11], we therefore refer to these emission features as two-photon-induced photoluminescence (2P-PL). The discretization of the 2P-PL stems for the polariton mode quantization, in the direction perpendicular to the monolayer extension as presented in Figure 1e in the main text and the peak separation 3.1 meV is in agreement with the model introduced in S5. The non-linear nature of the two photon absorption process is directly reflected in figure S5b, where we plot the SHG emission intensity (excluding 2P-PL) at double the excitation energy as a function of the excitation power in a double-logarithmic scale. The extracted power law coefficient of 1.997 clearly confirms the two-photon absorption nature of the process, and unambiguously demonstrates the highly non-linear properties of our strongly coupled device. We further study the emission intensity at double the excitation energy (orange marked feature in figure S5a) as a function of the orientation of the linearly polarized excitation light. As previously shown[12], in case of experiments carried out on bare monolayers, we observe an intensity modulation with a 60°-periodicity which stems from the SHG selection rules for the three-fold crystal symmetry.

S7: SHG on bare $MoSe_2$ monolayer

In order to extract the SHG characteristics that arise from the monolayer, we probed a bare $MoSe_2$monolayer encapsulated in h-BN at 1509 nm and compare the SHG spectrum to conventional PL (532 nm excitation) as presented in figure S5. While exciton and trion resonances exhibit linewidths of 8 – 10 meV, the SHG signal carries the laser linewidth of about 3 meV.

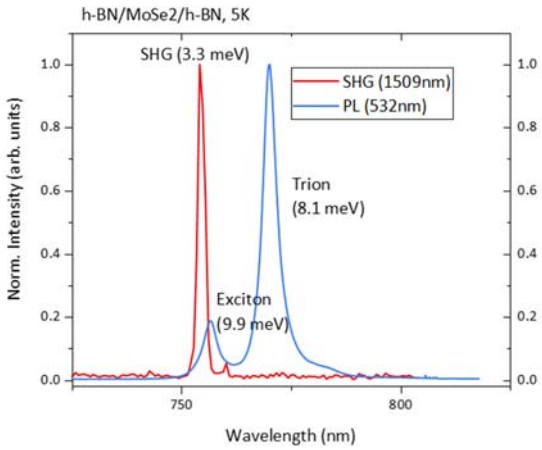

Figure S6: Comparison of the photoluminescence (in blue) and SHG (in red) response of bare $MoSe_2$ monolayer

S8: Radiative lifetime of the exciton-polaritons

The radiative polariton lifetime $\tau_{polariton}$ can be estimated based on the exciton lifetime $\tau_{exciton}$ and cavity lifetime τ_{cavity}. The lifetime is calculated according to[13]:

$$\frac{1}{\tau_{polariton}} = |X|^2 \frac{1}{\tau_{exciton}} + |C|^2 \frac{1}{\tau_{cavity}} \quad (1)$$

Where $|X|^2$ (0.26) and $|C|^2$ (0.74) are the exciton and cavity fractions of the polariton, respectively (taken from S2). The exciton lifetime $\tau_{exciton}$ is estimated to be 390 fs[14] and the cavity lifetime τ_{cavity} is calculated according to

$$\tau_{cavity} = \frac{h}{4\pi\Delta E} \quad (2)$$

Where h is Planck's constant and ΔE is the cavity linewidth. This yields 170 fs for τ_{cavity} with a ΔE of 1.54 meV (equivalent to a Q factor of 1030), taken form the reflectivity spectrum in Fig. 1c in the main text. Finally, a polariton radiative lifetime of 199 fs is extracted.

S9: Second Harmonic Generation Selection rules

Figure 2e and f in the main text depict the experimentally acquired spectra and calculated DOLP values. According to the SHG selections rules[5], the SHG polarization plane is rotated by 2θ in opposite direction, with θ being the angle between the orientation of the linear excitation and the crystal axis.

To understand the effect in more detail we note that TMDC ML is described by the D_{3h} point symmetry.

Let the horizontal reflection plane be (*xy*) (i.e., the monolayer is in the (*xy*) plane) and the vertical reflection plane be $\sigma_v||(xz)$ (i.e., the reflection *y*→−*y* is possible). Thus, phenomenological equations for the linearly polarized excitation describing the second harmonic generation read

$$P_x = \chi(E_y^2 - E_x^2) = \chi|E|^2\cos(2\theta)\,, \quad P_y = -2\chi E_x E_y = -\chi|E|^2\sin(2\theta)\,,$$

where χ is the only non-zero component of the second-order susceptibility tensor.

In the particular case of the X polarization $\theta = 0°$, which means that the SHG polarization plane is aligned with the linear excitation orientation. This is confirmed in the polarization resolved measurements, showing a strongly polarized signal in X polarization. At the energy of double the excitation photon, this is a direct consequence of the SHG selection rule. In the case of the Y excitation, $\theta = 30°$ meaning that the SHG polarization plane is rotated by $-60°$ with respect the nearest crystal axis, which ultimately leads to an SHG orientation in the X configuration. In fact, at the energy of double the excitation energy, the signal measured in the X configuration is slightly stronger than in Y. However, all other features of the spectrum are strongly polarized in the Y basis, meaning that the two-photon interband transition and the subsequent 2P-PL follow the initial excitation. This analysis is consistent with the observations in reference[7]. The described procedure is therefore a suitable way to distinguish between the two microscopic processes. The energy difference between excitation and emission from the polariton ground state and interband-transition process allows us to interpret the DOLP values of more than 90% as valley coherence.

S10: Polariton propagation length

An intensity profile was taken from the intensity distribution presented in Fig. S7a (see also Fig. 3a in the main text, profile cut is marked by the orange line), which is plotted in Figure S7b. This profile was fitted with a convolution of the Gaussian shaped focus profile (FWHM of 2.5 µm) and an exponentially decaying function. This fit yields a decay constant of 3.6 µm, which is taken as an estimate of the polariton propagation length.

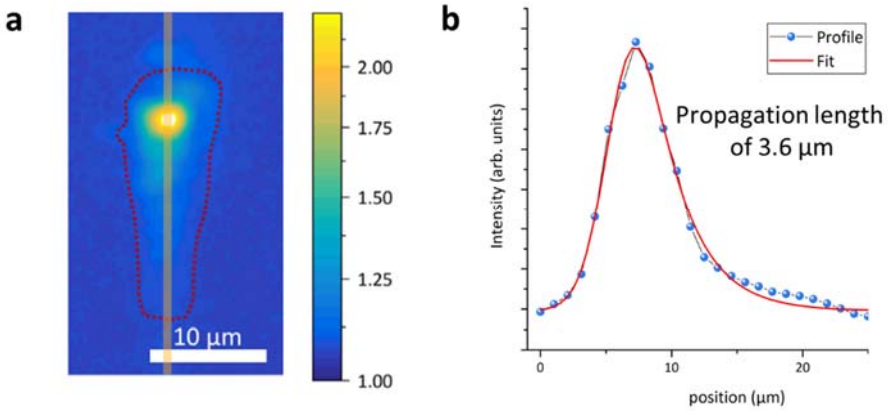

Figure S7: Polariton diffusion length: a) intensity distribution across the monolayer. The line of the profile that is presented in b) is marked in orange. The profile was fit with a convolution of a Gaussian shaped focus with an exponential decay function to extract a polariton propagation length of 3.6 µm.

S11: Details on the numerical modelling

To take the finite size of the TMD monolayer stripe into account and to simulate the confinement of polaritons both along and across the stripe, we take the stationary potential $V_0(\mathbf{r})$ in the form

$$V_0(\mathbf{r}) \propto 1 - e^{-\left[2(x-x_0)/w_x\right]^{12}} e^{-\left[2y/(1-\nu x)w_y\right]^6}, \tag{3}$$

where w_x and w_y are the length and the width of the stripe, x_0 is the distance along the x axis with respect to the position of the pump spot. The factor $(1-\nu x)$ describes the narrowing of the stripe. The smooth super-Gaussian shape of the potential is chosen to avoid possible numerical issues in the simulations caused by an abrupt variation of the potential landscape, see e.g. Ref.[15].

The pump is taken in the Gaussian form

$$P_\sigma(\mathbf{r}) \propto e^{-[x^2+(y-y_1)^2]/2w_p^2} e^{-i\omega_p t}, \tag{4}$$

where w_p is the pump width, $\hbar\omega_p$ is the pump energy. The parameter y_1 is used to take into account the slight shift of the pump spot from the central axis of the stripe.

S12: Polarization patterns without confinement

Formation of the polarization patterns is determined to the greatest extent by the pseudospin evolution under the spin-orbit coupling. Neither a spatial confinement potential nor non-conservative processes lead to significant qualitative changes of the spatial distribution of the polarization. Let us consider the system described by the linear Hamiltonian $\hat{H}_\mathbf{k}$ in the effective mass approximation:

$$\hat{H}_\mathbf{k} = \begin{bmatrix} \hbar^2k^2/2m_{\text{eff}} & \Delta k^2 e^{-2i\theta} \\ \Delta k^2 e^{2i\theta} & \hbar^2k^2/2m_{\text{eff}} \end{bmatrix}, \tag{5}$$

where θ is the angle of injection characterizing the $\mathbf{k}$-state as $\mathbf{k} = \left(k\cos(\theta), k\sin(\theta)\right)$. Δ is the splitting constant, m_{eff} is the polariton effective mass. Here, we neglect both confinement and non-conservative processes. The Hamiltonian (5) can be rewritten in terms of the effective magnetic field $\mathbf{\Omega}_\mathbf{k} = (\Omega_{x,\mathbf{k}}, \Omega_{y,\mathbf{k}}, 0)$ acting on the polariton pseudospin:

$$\hat{H}_\mathbf{k} = \frac{\hbar^2k^2}{2m_{\text{eff}}}\hat{\sigma}_0 + \hbar\mathbf{\Omega}_\mathbf{k}\cdot\hat{\boldsymbol{\sigma}} = \frac{\hbar^2k^2}{2m_{\text{eff}}}\hat{\sigma}_0 + \hbar(\Omega_{x,\mathbf{k}}\hat{\sigma}_x + \Omega_{y,\mathbf{k}}\hat{\sigma}_y), \tag{6}$$

where the components of $\mathbf{\Omega}_\mathbf{k}$ are given as $\Omega_{x,\mathbf{k}} = \Delta k^2\cos(2\theta)$, $\Omega_{y,\mathbf{k}} = \Delta k^2\sin(2\theta)$. $\hat{\boldsymbol{\sigma}} = (\hat{\sigma}_x, \hat{\sigma}_y, \hat{\sigma}_z)$ is the vector of the Pauli matrices. The Hamiltonian $\hat{H}_\mathbf{k}$ yields to the following precession equation for the pseudospin vector $\mathbf{S}_\mathbf{k} = \langle\hat{\boldsymbol{\sigma}}\rangle = (S_{x,\mathbf{k}}, S_{y,\mathbf{k}}, S_{z,\mathbf{k}})$ around the effective magnetic field:

$$d_t\mathbf{S}_\mathrm{k} = \mathbf{\Omega}_\mathbf{k} \times \mathbf{S}_\mathbf{k}. \tag{7}$$

For the linear initial polarization, $S_{z0} \equiv S_{z,\mathbf{k}}(0) = 0$, the circular polarization evolution can be found from Eq. (7) analytically:

$$S_{z,\mathbf{k}}(t) = \frac{1}{\Omega}\left(\Omega_{x,\mathbf{k}} S_{y0} - \Omega_{y,\mathbf{k}} S_{x0}\right)\sin(\Omega t), \tag{8}$$

where $\Omega = |\mathbf{\Omega}|$ is the Larmor frequency. From the general solution (8) of Eq. (7) we can find spatial distribution of the degree of the circular polarization (DOCP) along the sample, considering the polariton state with the wave vector $\mathbf{k}_1 = (k,0)$:

$$S_{z,\mathbf{k}_1}(t) = S_{y0}\sin(\Delta k^2 t), \tag{9}$$

which reduces to $S_{z,\mathbf{k}_1}(t) \approx S_{y0}\Delta k^2 t$ close to the injection spot.

The solution (8) allows also to predict the polarization variation across the sample. We consider the case of a point-like source of polaritons, possessing the wave number k. Polaritons in the $\mathbf{k}$-state reach the crossection spaced by a distance L_x from the injection spot in time of $T(\theta) = L_x / v_x \propto 1/k\cos(\theta)$. The resulting DOCP distribution in this crossection is found as

$$\begin{aligned} S_{z,\mathbf{k}}\left(T(\theta)\right) &= \frac{1}{\Omega}\left(\Omega_{x,\mathbf{k}} S_{y0} - \Omega_{y,\mathbf{k}} S_{x0}\right)\sin\left(\Omega T(\theta)\right) \\ &\approx \left(\Omega_{x,\mathbf{k}} S_{y0} - \Omega_{y,\mathbf{k}} S_{x0}\right) T(\theta) \propto \frac{S_{y0}\cos(2\theta) - S_{x0}\sin(2\theta)}{\cos(\theta)}. \end{aligned} \tag{10}$$

Figure S8 allows comparing the numerical simulations and the analytical predictions of the spatial distribution of DOCP for different angles of the initial polarization plane. The panels show the simulated DOCP distributions (left). The right upper panels show the color bars illustrating the expected DOCP distribution across the sample found from Eq. (10). Approximate position of the crossection is labeled by the green dashed line in the left figure. The right lower panels show the diagram showing the dominating polarization in the plane of the sample calculated according to Eq. (9). The dash-dotted line in the left panel shows the examined direction. The dash-dotted line in the right lower figure indicates the circular polarization degree expected.

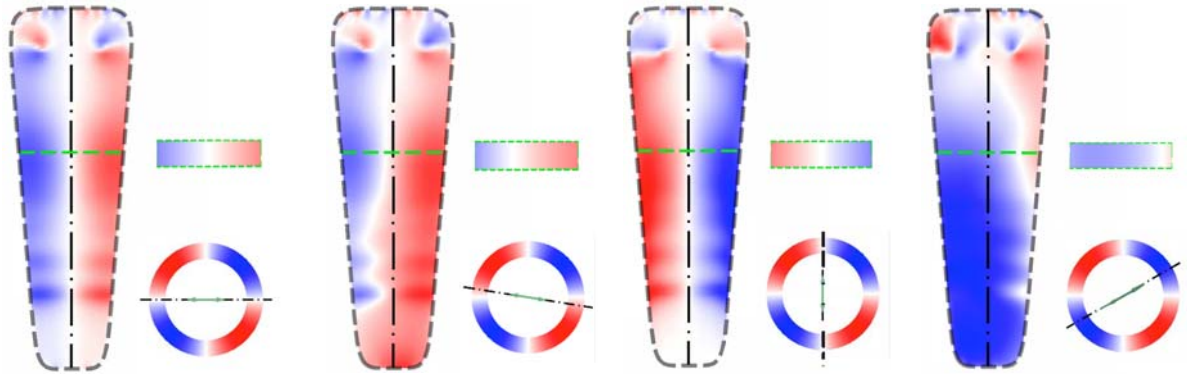

Figure S8: Simulated and analytically calculated spatial distribution of the DOCP for various polarization orientations.

S13:Polariton pattern in a stipe

We consider a stripe where polaritons can propagate along y axis while their motion along x axis is quantized. With account for the TE-TM splitting the effective Hamiltonian in the basis of the *linearly* polarized states reads

$$\mathcal{H} = \frac{\hbar^2 k^2}{2m}\hat{I} + \Delta\begin{pmatrix} k_x^2 - k_y^2 & 2k_x k_y \\ 2k_x k_y & k_y^2 - k_x^2 \end{pmatrix}. \quad (11)$$

Here $\hat{I}$ is the unit 2×2 matrix, m is the polariton effective mass, Δ is the TE-TM splitting parameter (which weakly depends on the polariton wavevector k). The Hamiltonian can be rewritten as

$$\mathcal{H} = \frac{\hbar^2}{2m}\begin{pmatrix} (1+\alpha)k_x^2 + (1-\alpha)k_y^2 & 2\alpha k_x k_y \\ 2k_x k_y & (1+\alpha)k_y^2 + (1-\alpha)k_x^2 \end{pmatrix}, \quad (12)$$

where $\alpha = 2m\Delta/\hbar^2$.

Zero-order approximation. Single subband model. We introduce the basic states

$$|x\rangle = \begin{pmatrix} 1 \\ 0 \end{pmatrix}, \quad |y\rangle = \begin{pmatrix} 0 \\ 1 \end{pmatrix},$$

and write the wavefunctions functions as (the normalization length is set to unity)

$$\Psi_x = e^{\mathrm{i}k_y y}\cos\left(\frac{\pi x}{L}\right)|x\rangle, \quad \Psi_y = e^{\mathrm{i}k_y y}\cos\left(\frac{\pi x}{L}\right)|y\rangle. \quad (13)$$

The dispersions of these states are given by

$$E_x(k_y) = \frac{\hbar^2\pi^2}{2mL^2}(1+\alpha) + \frac{\hbar^2 k_y^2}{2m}(1-\alpha), \quad (14)$$

$$E_y(k_y) = \frac{\hbar^2\pi^2}{2mL^2}(1-\alpha) + \frac{\hbar^2 k_y^2}{2m}(1+\alpha). \quad (15)$$

The TE-TM splitting of the states reads

$$\Delta_{TE-TM}(k) = \alpha\frac{\hbar^2}{m}\left(\frac{\pi^2}{L^2} - k_y^2\right), \quad (16)$$

and contains contributions due to the wavevector and due to the size-quantization.

The wavefunctions (13) correspond to definite linear polarization. In order to obtain the mixing of polarizations and circular polarization of polaritons, we need to account for the off-diagonal terms in Eq. (12).

First-order approximation. Let us calculate the correction to the Ψ_x due to the off-diagonal terms. The represent

$$\Psi_x = e^{\mathrm{i}k_y y}\left[\cos\left(\frac{\pi x}{L}\right)|x\rangle + S(x)|y\rangle\right], \quad (17)$$

where $S(x)$ is the function which satisfies the equation

$$\left[\frac{\hbar^2}{2m}\frac{d^2}{dx^2} - E_x(k_y)\right]S(x) = -\mathrm{i}\alpha\frac{\hbar^2\pi k_y}{mL}\sin\left(\frac{\pi k_y}{L}\right). \quad (18)$$

The solution reads

$$S(x) = -\frac{\mathrm{i}\alpha\hbar^2\pi k_y}{mL\left[\frac{\hbar^2\pi^2}{mL^2} - 2E_x(k_y)\right]}\left[\sin\left(\frac{\pi x}{L}\right) - \frac{\sin\left(\sqrt{2mE_x(k_y)/\hbar}x\right)}{\sin\left(\sqrt{mE_x(k_y)/2\hbar}L\right)}\right]. \quad (19)$$

Neglecting α and k_y dependence of $E_x(k_y)$ we have for the admixed function a much simpler expression

$$S(x) = -\alpha k_y x \cos\frac{\pi x}{L}. \tag{20}$$

The circular polarization degree in the state Ψ_x is given, in the first order in α, by

$$P_c(x, k_y) = \frac{2S(x)\cos\frac{\pi x}{L}}{\cos^2\frac{\pi x}{L}} \approx -\alpha k_y x. \tag{21}$$

For the second state Ψ_y the circular polarization degree $P_c(x, k_y) \approx \alpha k_y x$.

S14:Experimental DOCP patterns at intermediate angles

In addition to the DOCP patterns in the main text, we have recorded further patterns at intermediate excitation polarization angles. Most polarization angles result in a net circular polarization with respect the DOCP recorded at the excitation spot. Figure S9 presents the net DOCP as a function of the excitation polarization angle. Here, the intensity maxima (excitation spot center) of the σ^+ and σ^- measurements were taken to calculate the net DOCP. We attribute this net polarization to the spin-anisotropic stimulated scattering into a polariton ground state from the more weakly polarized exciton reservoir, which certainly occurs in the system. The authors of Ref. [16] report on the strong correlation between the ellipticity of the non-resonant optical pump and the degree of circular polarization of the polariton condensate in a conventional semiconductor DBR microcavity. They demonstrate the increase of the DOCP of the polariton condensate up to tens of percent under the pump with a slight ellipticity not exceeding 0.1. The linearly polarized pump beam acquires and accumulates ellipticity when passing through the top DBR mirror before excite excitons in a quantum well. We have also observed the similar effect in a recent work [17].

Figure S10 shows the measured and modelled polarization patterns of expanding polaritons in our channel for various angles of initialization. To account for the net DOCP polarization, we set the red-to-blue transition of the color scale to corresponding net DOCP value (figure S9). Clearly, we observe the consistently rotating polarization pattern as the hallmark feature of the OVHE.

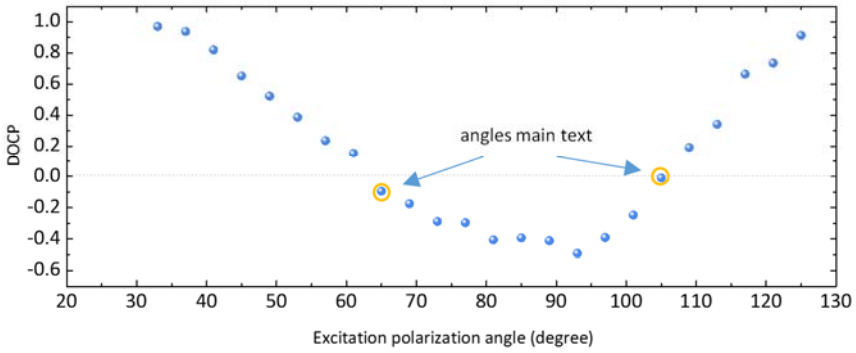

Figure S9: Net DOCP as a function of the excitation polarization angle. The net DOCP is determined by the σ^+ and σ^- maximum intensity values (at the excitation spot center).

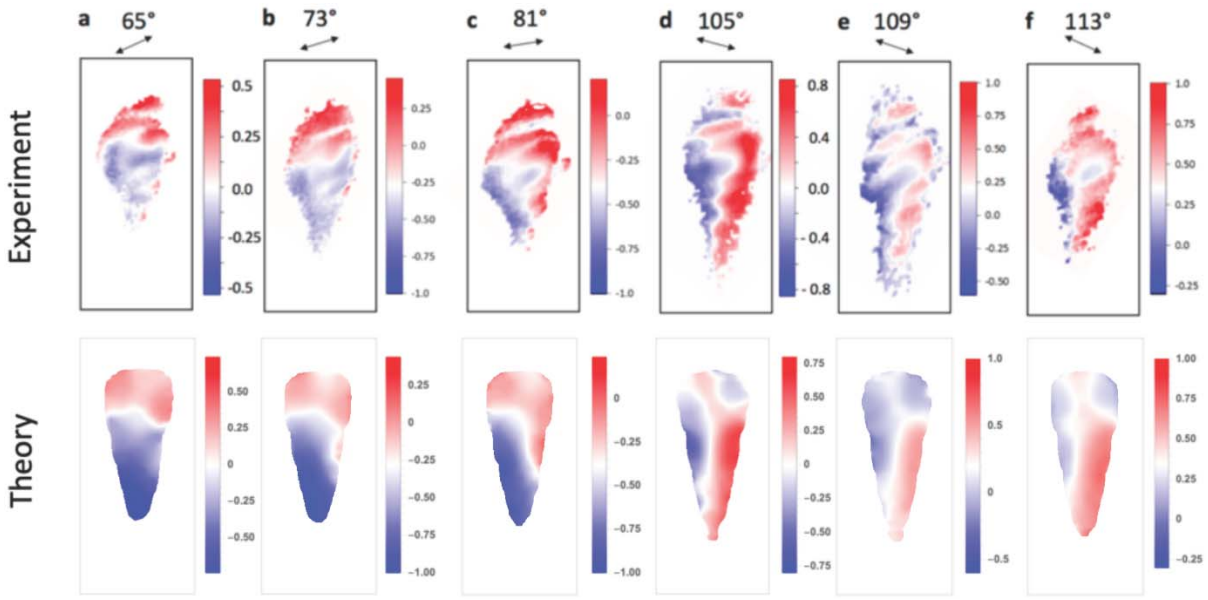

Figure S10: Spatial DOCP distribution along the monolayer for various angles. The upper line shows measured distributions, where the red-to-blue transitions of the color scales correspond to the net DOCP value for each angle. The lower line presents the corresponding theoretically modelled distributions.

S15:Experimental DOCP patterns utilizing linear spectroscopy

In addition to the polarization patterns presented in the main text of the manuscript and figure S10, we have confirmed our results signifying valley Hall behaviour by injecting polaritons in our system utilizing a continuous wave pump laser with a wavelength of 740 nm (slightly blue-detuned from the exciton resonance). Under such experimental conditions, we note that we were not able to record pronounced effects of valley polarization and coherence such as reported in Fig. 3 in the main text, but results are consistent with the literature (on the order of 10-30 %, e.g. Ref. 18).

Under such conditions, we capture qualitatively similar, yet significantly less pronounced polarization patterns in our microcavity upon linear polarized excitation, which are plotted in fig S11.

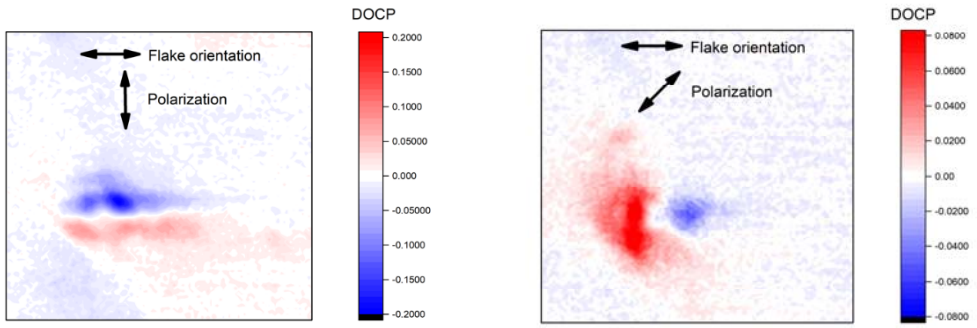

Figure S11: Spatial DOCP distribution along the monolayer following polariton injection with a linear polarized pump laser, slightly blue detuned from the exciton resonance. We capture clear polarization patterns, which qualitatively follow the expected geometric behaviour plotted in S8, and which turns with rotating initial polarization. We note, that the degrees of circular polarization in this configuration are strongly reduced, compared to the case of two-photon quasi-resonant injection (main text).

References:

1. Schmutzler, J. *et al.* Nonlinear spectroscopy of exciton-polaritons in a GaAs-based microcavity. *Phys. Rev. B - Condens. Matter Mater. Phys.* **90,** 1–6 (2014).
2. Stier A. et al. Exciton diamagnetic shifts and valley Zeeman effects in monolayer WS_2 and MoS_2 to 65 Tesla *Nature communications* 7 (2016).
3. Lundt, N. *et al.*, Magnetic field induced splitting and polarization of monolayer-based valley polaritons *arxiv.*, 05250 (2019).
4. Fischer, J., et al. "Anomalies of a nonequilibrium spinor polariton condensate in a magnetic field. *Physical review letters* 112 093902 (2014).
5. Lundt, N. *et al.*, Monolayered MoSe2: a candidate for room temperature polaritonics. *2D Mater.* **4**, 015006 (2017).
6. Sidler, M. *et al.* Fermi polaron-polaritons in charge-tunable atomically thin semiconductors. *Nat. Phys.* **13,** 255-261 (2017).
7. Chakraborty, B. *et al.* Control of Strong Light–Matter Interaction in Monolayer WS2 through Electric Field Gating. *Nano Lett.* **18,** 6455–6460 (2018).
8. Tartakovskii, A. I., Kulakovskii, V. D., Forchel, A. & Reithmaier, J. P. Exciton-photon coupling in photonic wires. **57,** 6807–6810 (1998).
9. Glazov, M. M. *et al.* Intrinsic exciton-state mixing and nonlinear optical properties in transition metal dichalcogenide monolayers. *Phys. Rev. B* **95,** 35311 (2017).
10. Gong, P., Yu, H., Wang, Y. & Yao, W. Optical selection rules for excitonic Rydberg series in the massive Dirac cones of hexagonal two-dimensional materials. Phys. Rev. B **95**, 125420 (2017).
11. Seyler, K. L. Electrical control of second-harmonic generation in a WSe_2 monolayer transistor. *Nat. Nanotechnol.* **10,** 407–411 (2015).
12. Malard, L. M., Alencar, T. V, Barboza, A. P. M., Mak, K. F. & Paula, A. M. De. Observation of intense second harmonic generation from MoS 2 atomic crystals. *Phys. Rev. B* **87,** 201401(R) (2013).
13. Deng, H., Haug, H. & Yamamoto, Y. Exciton-polariton Bose-Einstein condensation. *Rev. Mod. Phys.* **82,** 1489–1537 (2010).
14. Jakubczyk, T. *et al.* Radiatively Limited Dephasing and Exciton Dynamics in MoSe 2 Monolayers Revealed with Four-Wave Mixing Microscopy. *Nano Lett.* **16,** 5333–5339 (2016).
15. Slavcheva, G., Gorbach, A. V, Pimenov, A., Vladimirov, A. G. & Skryabin, D. V. Multi-stability and polariton solitons in microcavity wires. *Optics Lett.* **40,** 1787–1790 (2015).
16. Askitopoulos, A., Kalinin, K., Liew, T. C. H., Cilibrizzi, P., Hatzopoulos, Z., Savvidis, P. G., Berloff, N. G. and Lagoudakis P. G., Nonresonant optical control of a spinor polariton condensate. *Phys. Rev. B* **93**, 205307 (2016).
17. Lundt, N., Sedov, E., Waldherr, M., Klaas, M., Knopf, H., Blei, M., Tongay, S., Klembt, S., Taniguchi, T., Watanabe, K., Schulz, U., Kavokin, A., Höfling, S., Eilenberger, F, Schneider, C., Magnetic field induced splitting and polarization of monolayer-based valley exciton-polaritons, arXiv:1901.05250
18. Dufferwiel, S. *et al.* Valley-addressable polaritons in atomically thin semiconductors. *Nat. Photonics* **11,** 497–501 (2017)).